

Croton macrostachyus Leaf Extract-Mediated Green Synthesis of ZnO Nanoparticles and ZnO/CuO Nanocomposites for the Enhanced Photodegradation of Methylene Blue Dye with the COMSOL Simulation Model

Solomon Bekele Endeshaw, Lemma Teshome Tufa, Mahendra Goddati, Jaebeom Lee, Vanna Christmas Silalahi, Donghan Lee, H. C. Ananda Murthy,* and Fedlu Kedir Sabir*

Cite This: *ACS Omega* 2024, 9, 559–572

Read Online

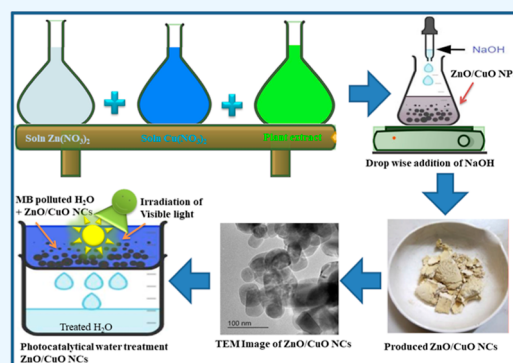
ACCESS |

Metrics & More

Article Recommendations

Supporting Information

ABSTRACT: The photodegradation of organic pollutants using metal oxide-based catalysts has drawn great attention as an effective method for wastewater treatment. In this study, zinc oxide nanoparticles (ZnO NPs) and zinc oxide/copper oxide nanocomposites (ZnO/CuO NCs) were fabricated using the leaf extract of *Croton macrostachyus* as a nontoxic, natural reducing and stabilizing agent. The synthesized samples were characterized by employing X-ray diffraction, microscopic, spectroscopic, and electrochemical methods. The results confirmed the successful synthesis of ZnO NPs and ZnO/CuO NCs with well-defined crystalline structures and morphologies. The prepared samples were tested for the photodegradation of methylene blue (MB) dye under visible light irradiation. Compared to ZnO NPs, ZnO/CuO NCs showed greatly improved photocatalytic performances, particularly with the sample prepared with the 20 mol % Cu precursor (97.02%). The enhancement could be related to the formed p–n heterojunction, which can suppress the recombination of charge carriers and extend the photoresponsive range. A theoretical study of the photocatalytic activity of ZnO/CuO NCs against MB dye degradation was also conducted by using COMSOL Multiphysics software. The results of the simulation are in reasonable agreement with those of the experiment. This study contributes to the development of sustainable and effective photocatalytic materials that are suitable for application in environmental remediation, particularly in the treatment of wastewater.



1. INTRODUCTION

Environmental problems associated with water contamination are very significant issues correlated negatively with human health and the ecosystem. The uncontrolled release of contaminated wastewater from various industries has led to serious environmental contamination. In particular, various recalcitrant organic pollutants, such as pesticides and dyes, are carcinogenic and toxic and pose a serious hazard to human and aquatic life.¹ The current conventional water treatment methods are expensive, complex, and inefficient for the complete degradation of persistent organic pollutants.^{1–3} Thus, more efficient, low-cost, and eco-friendly techniques are needed to remove these contaminants from wastewater. Photocatalytic degradation of water pollutants by solar energy is a reliable way for environmental remediation with minimal associated costs.^{4,5} Heterogeneous photocatalysis on semiconducting metal oxide nanoparticles (NPs) is a promising and sustainable process for the removal of various organic and inorganic contaminants from water using abundantly available solar light irradiation,^{6–8} while its viability, in practice, is highly dependent on effective photocatalysts.

Among various well-known metal oxide NPs, ZnO has been intensively investigated for photocatalytic purification of wastewater due to its nontoxicity, chemical stability, low price, abundant availability, green characteristics, and large exciton binding energy.^{9,10} However, the fast recombination of photogenerated charge carriers and a low response to visible light limit the photocatalytic activity of ZnO in practice.^{11,12} In order to overcome the limitations faced by pristine ZnO, several modifications aimed at enhancing the spectral response and the charge-separation efficiency have been employed by different researchers. Among the various studied approaches, the formation of composites with other narrow band gap semiconductors or with other nanostructured materials such as noble metals or graphene has been reported as the most

Received: August 19, 2023
Revised: November 19, 2023
Accepted: November 27, 2023
Published: December 19, 2023



promising strategy to improve the photocatalytic activity of ZnO.^{11–14} In particular, the coupling of n-type ZnO with p-type narrow-bandgap CuO to form a p–n heterojunction has been considered an effective approach to suppress the e^- – h^+ recombination and to optimize the photoresponding range. Many researchers have reported on the enhanced photoactivity of ZnO/CuO NCs with respect to pristine ZnO and CuO for photodegradation of various pollutants under UV as well as visible light irradiation.^{14–20} Recently, Maru et al. prepared zinc oxide NPs (ZnO NPs), CuO NPs, and CuO/ZnO NCs by the green route using the extract of *Musa acuminata* peel and investigated their photocatalytic activities toward methylene blue (MB) dye degradation under visible light irradiation. The results revealed the enhanced photocatalytic performance of CuO/ZnO NCs relative to pure ZnO and CuO NPs.²¹ Similarly, Bekru et al. reported that the CuO/ZnO NCs prepared by the microwave-assisted green method showed higher activity for photocatalytic degradation of MB than that of their pure counterparts under UV and visible light irradiation. This high activity was attributed to the enhanced photogenerated charge carrier separation and transfer caused by the band coupling between ZnO and CuO.²²

The preparation of ZnO NPs as well as ZnO-based nanocomposites (NCs) has been carried out by various well-known methods such as sol–gel,²³ hydrothermal and solvothermal,^{24,25} precipitation,²⁶ electrochemical,^{27,28} thermal decomposition,¹⁵ microwave-assisted,²⁹ and spray pyrolysis.³⁰ However, the above-mentioned synthesis techniques are expensive, complex, and toxic to the environment due to the association of various hazardous chemicals³¹ as reducing and stabilizing agents. In recent times, the biological approach for fabricating nanomaterials using naturally available bioentities such as microorganisms and plants has gained much attention owing to its nontoxicity, environmental benignity, and low cost.^{32,33} Among natural materials, plant extracts are considered the best choice for biosynthesis of NPs and NCs due to the availability of abundant and potent phytochemicals contained in them.^{33,34} The bioactive compounds existing in the plant, such as polyphenols, flavonoids, steroids, tannins, alkaloids, etc., can serve as strong bioagents for the reduction and/or stabilization of NPs during their synthesis.^{32–34}

Up to now, various metal oxides, such as ZnO and CuO NPs, and their NCs have been prepared by employing different kinds of plant extracts, such as *Lippia adoensis*,³⁵ *Tabernaemontana divaricate*,³⁶ *Becium grandiflorum*,³⁷ *Azadirachta indica*,³⁸ *Pandanus odorifer*,³⁹ *Psidium guajava*,⁴⁰ *Verbascum thapsus*,⁴¹ *Mentha longifolia*,⁴² *Calotropis gigantean*,⁴³ *Aloe barbadensis*,⁴⁴ and *Alchornea cordifolia*.⁴⁵ Metal oxide NPs and their NCs fabricated through a plant extract-mediated biosynthesis approach are ascertained to be notably efficient for antibacterial as well as photodegradation applications compared to those of chemically synthesized NPs and NCs. In this regard, using green methods in the synthesis of zinc oxide-based NCs has increasingly become a necessity.

Croton macrostachyus plant belongs to the family *Euphorbiaceae* and is also known as Bisana, rush foil, etc. It is a broad-leaved tree which is commonly widespread in Ethiopia, Eretria, Kenya, Tanzania, and Uganda.^{46,47} The different parts of *C. macrostachyus* have been reported to show various pharmacological effects, such as antimicrobial, antioxidant, antifungal, antiplasmodial, antidiabetic, etc.^{47–56} Phytochemical screening of the plant leaf showed the existence of secondary metabolites, such as phenolic compounds, steroids, terpenoids,

aponins, tannins, alkaloids, flavonoids, and free anthraquinones.^{51–58} Therefore, the leaf extract of this plant can be used as an eligible source of reducing and stabilizing agents for the biosynthesis of NPs.

In this study, the leaf extract from *C. macrostachyus* was employed for the first time as a nontoxic, eco-friendly, and natural reducing and stabilizing agent to synthesize pristine ZnO NPs and binary ZnO/CuO NCs. As reported in the literature,^{51–58} the employed plant is rich in multiple classes of potent phytochemicals, which are favorable for efficient bioreduction and stabilization of NPs. Moreover, this plant is abundantly available and cost-effective. However, despite its multiple advantages and natural abundance, *C. macrostachyus* has not been employed to synthesize ZnO NPs and ZnO/CuO NCs in previous research. In fact, our results clearly confirm the inherent capacity of *C. macrostachyus* for the size as well as morphology-controlled green synthesis of ZnO NPs and ZnO/CuO NCs in a simple, rapid, cost-effective, and eco-friendly way. The prepared ZnO NPs and ZnO/CuO NCs were characterized using different sophisticated characterization techniques. The photocatalytic performance of the synthesized samples was investigated for the photodegradation of MB dye under visible light irradiation. In addition, the three-dimensional (3D) theoretical model was also developed on the basis of experimental conditions using COMSOL software to simulate the photocatalytic activity of ZnO/CuO NCs.

2. MATERIALS AND METHOD

2.1. Materials and Chemicals. The chemical reagents employed in this work, including zinc nitrate hexahydrate ($Zn(NO_3)_2 \cdot 6H_2O$, 99%), copper nitrate trihydrate ($Cu(NO_3)_2 \cdot 3H_2O$, 99%), and sodium hydroxide (NaOH, 99%), with AR grade, were obtained from Sigma-Aldrich and Merck and used directly without any additional purification. MB ($C_{16}H_{18}ClN_3S$) dye was utilized for the photodegradation efficiency test. Distilled water was employed throughout all conducted experiments.

2.2. Preparation of the Extract. The plant leaves of *C. macrostachyus* were collected from the East Shoa Zone, Adama, Oromia Regional state, Ethiopia. The collected fresh leaves were cleaned 2–3 times using distilled water to get rid of dust and other impurities and then dried at ambient conditions for 6 days, followed by crushing into fine powder using a grinder. Afterward, 10 g of the *C. macrostachyus* leaf powder was mixed with 200 mL of distilled water and stirred for 1 h at 70 °C. After cooling, the supernatant was separated by filtration and stored in the refrigerator to be used in subsequent syntheses.²¹

2.3. Preparation of the Nanomaterials. **2.3.1. Chemical Synthesis of ZnO NPs.** The chemically synthesized ZnO NPs sample was fabricated using a simple coprecipitation method, as reported by Thambidurai et al.²⁵ with some modifications. Briefly, 10.41 g of $Zn(NO_3)_2 \cdot 6H_2O$ was mixed with 175 mL of distilled water under vigorous stirring to achieve a 0.2 M aqueous solution concentration. The NaOH (2 M) solution was then added in a dropwise manner into the above solution with constant vigorous magnetic stirring at 60 °C so as to reach pH \approx 11. A milky white solution with a white precipitate was formed. The resulting white solution was stirred further for another 1 h at 60 °C; then, it was cooled and aged for 20 h at ambient temperature. The white suspension was filtered, washed with ethanol and distilled water sequentially, and then oven-dried at 80 °C for 20 h. Finally, the dried product was subjected to furnace calcination at 450 °C for 2 h. In this

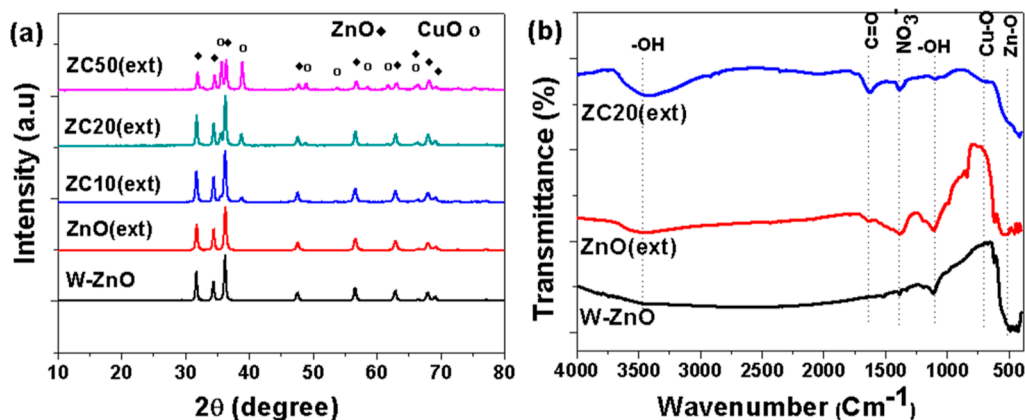


Figure 1. (a) Powder XRD diffractograms and (b) FT-IR spectra of the prepared samples.

paper, the obtained chemically synthesized ZnO was denoted as W-ZnO.

2.3.2. Green Synthesis of ZnO NPs. To synthesize the green-mediated ZnO NPs, 10.41 g of $\text{Zn}(\text{NO}_3)_2 \cdot 6\text{H}_2\text{O}$ was mixed with 150 mL of distilled water under constant stirring. Later, 25 mL of an aqueous extract of *C. macrostachyus* was slowly dripped into the above solution with vigorous stirring at 60 °C. After 30 min, a few drops of NaOH (2 M) solution were then added under stirring to adjust the pH, and the solution was continuously stirred for another 1 h at 60 °C. It was then cooled and aged for 20 h at room temperature for stabilization. The light yellow precipitate was separated by filtration, washed repeatedly with distilled water and ethanol, and subsequently was oven-dried at 80 °C for 20 h. The dried product was calcined at 450 °C for 2 h. For simplification, this green synthesized ZnO sample was denoted as ZnO(ext).⁴⁵

2.3.3. Green Synthesis of ZnO/CuO NCs. Three different binary ZnO/CuO NCs samples with 10, 20, and 50% CuO ratios were also prepared through a one-pot green approach, as described above. For the biosynthesis of the ZnO/CuO (50%) NCs, 10.41 g of zinc nitrate and 8.45 g of copper nitrate were dissolved in 150 mL of distilled water under stirring. 25 mL of an aqueous extract of *C. macrostachyus* was added slowly into the above mixture while being stirred at 60 °C. The stirring continued for 30 min at 60 °C, and then a few drops of NaOH (2 M) solution was added to adjust the pH of the reaction mixture. The mixture was further stirred for 1 h at 60 °C and was cooled and aged for 20 h under ambient conditions. The dark brown suspension was filtered and washed repeatedly with distilled water and ethanol. The resulting solid was dried at 80 °C for 20 h and then calcined at 450 °C for 2 h. In the case of the ZnO/CuO (20%) and ZnO/CuO (10%) NCs, the amounts of copper nitrate were 2.11 and 0.94 g, respectively, with 10.41 g of zinc nitrate, and the above experimental steps were repeated. The obtained products were labeled as ZC10(ext), ZC20(ext), and ZC50(ext) for green synthesized ZnO/CuO(10%), ZnO/CuO(20%), and ZnO/CuO(50%) NCs samples, respectively.⁴⁵

2.4. Characterization Techniques. The prepared pristine ZnO NPs and binary ZnO/CuO NCs were characterized by using different techniques. The purity, crystallinity, and average crystalline size of the synthesized samples were examined by an X-ray diffraction (XRD)-700 Shimadzu X-ray diffractometer ($\lambda_{\text{CuK}\alpha} = 0.15406$ nm) in the 2θ range of 10–80°. The functional groups related to the fabricated NPs and NCs were identified by FT-IR analysis (FTIR, PerkinElmer 65) in the

scanning range of 400–4000 cm^{-1} . The surface morphology of all the synthesized samples was analyzed using SEM (Hitachi S-4800). The energy dispersive X-ray (EDX) system on the SEM was also utilized to analyze the elemental composition of the representative green-mediated ZnO/CuO NC. Furthermore, to analyze the shape, particle size, and crystallinity, the biosynthesized ZnO/CuO NC was studied using transmission electron microscopy (TEM) (Tecnai G2, FEI). Thermo Scientific X-ray photoelectron spectroscopy (XPS) ($\text{Al K}\alpha$ ($h\nu = 1350$ eV)) was also used to investigate the surface chemical composition and binding state of the biosynthesized ZnO/CuO NCs. The characteristic UV–visible absorption spectra of the synthesized samples were obtained by using a UV–vis spectrophotometer (JASCO model V-670). A fluorescence spectrophotometer (Agilent Cary Eclipse) was employed to analyze the emission spectra of the samples. The Mott–Schottky analysis also was conducted using a standard three-electrode cell with the FTO-loaded catalyst as the working electrode, platinum wire as the counter electrode, and 0.1 M Na_2SO_4 solution as an electrolyte.

2.5. Photocatalytic Activity Test. MB dye was utilized as a model pollutant to evaluate the photocatalytic performance of the prepared ZnO NPs and ZnO/CuO NCs samples under visible light irradiation (using a 150 W halogen lamp as a light source). Briefly, 30 mg of catalyst was added into 100 mL of aqueous solution of MB dye (10 mg/L) and stirred in the dark state for a span of 40 min to achieve adsorption–desorption equilibrium before irradiation. Then, the resulting content was subjected to visible light irradiation for the photodegradation process. During the irradiation experiments, 5 mL of sample was taken out every 20 min for a total of 80 min and centrifuged to remove the solid catalyst from the sample suspension. Thereafter, the absorbance of the resulting clear supernatant was measured by means of a UV–vis spectrophotometer (Azzota: SM-1600). The photodegradation efficiency was calculated using eq 1¹⁷

$$\text{degradation (\%)} = \frac{C_0 - C_t}{C_0} \times 100\% \quad (1)$$

where C_0 and C_t represent the dye concentrations at irradiation time of $t = 0$ and $t = t$, respectively. Moreover, the photocatalytic dye degradation kinetics was also studied by employing the pseudo-first-order kinetic model, and the rate of photodegradation was determined using the following formula⁵⁹

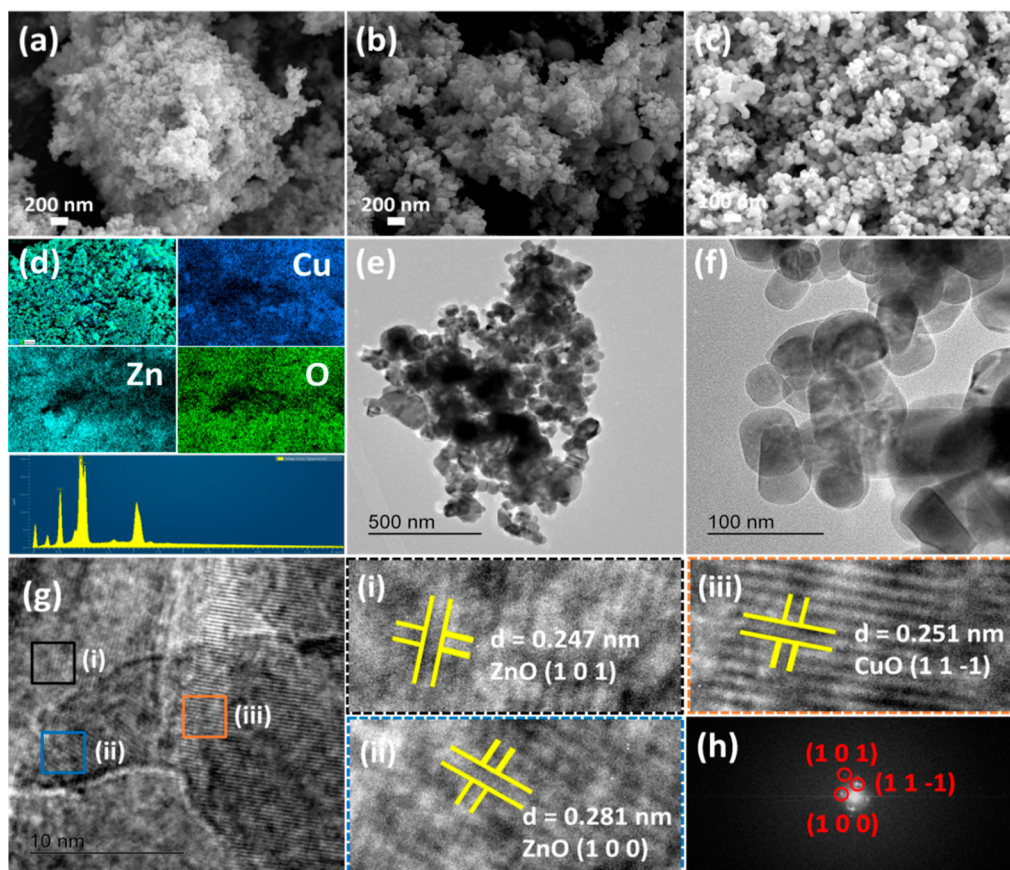


Figure 2. (a–c) SEM images of W–ZnO, ZnO(ext), and ZC50(ext) samples, respectively, (d) EDX element mapping image of ZC50(ext) NC, (e–g) TEM and HR-TEM images of ZC50(ext), and (h) FFT of (g).

$$\ln\left(\frac{C_t}{C_0}\right) = -kt \quad (2)$$

where C_0 and C_t stand for the dye concentrations at irradiation time of $t = 0$ and $t = t$, respectively, and k is the apparent reaction rate constant.

2.6. Computational Simulation of the Photocatalytic Activity of ZnO/CuO NCs. The photocatalytic activity of ZnO/CuO NCs against MB dye degradation was also simulated theoretically based on experimental conditions by employing the finite element method (FEM) using COMSOL Multiphysics software (version 6.1a). The radio frequency (RF), wave optics, and time-dependent modules in the COMSOL software were used to analyze the theoretically designed 3D model of the experimental circumstances. In this model, ZnO/CuO NCs have been considered a rigid and perfectly spherical particles of 30 nm diameter. The simulation of the photodegradation of MB dye ($n = 1.347$) by ZnO/CuO NCs was carried out with irradiation of electromagnetic (EM) waves in the visible wavelength range, and EM wave outcomes were collected at regular time intervals, as used in the experiment.

3. RESULTS AND DISCUSSION

3.1. XRD Analysis. The purity and the crystalline properties of the ZnO NPs prepared without plant extract (W–ZnO) and the green-mediated ZnO NPs (ZnO(ext)) and ZnO/CuO NCs (ZC10(ext), ZC20(ext), and ZC50(ext)) were characterized using powder XRD. Figure 1a shows XRD

patterns obtained for W–ZnO, ZnO(ext), ZC10(ext), ZC20(ext), and ZC50(ext) samples. As indicated in the figure, all of the peaks observed in the XRD pattern of ZnO(ext) showed similarity to that observed by W–ZnO. For both W–ZnO and ZnO(ext) samples, strong diffraction peaks at 31.8° (100), 34.4° (002), 36.3° (101), 47.6° (102), 56.6° (110), 62.9° (103), 66.4° (200), 67.9° (112), and 69.1° (201) revealed the hexagonal structure of ZnO (JCPDS, 36–1451),¹⁸ and no other peaks related to impurities were observed. On the other hand, for ZnO/CuO NCs samples other than the hexagonal ZnO peaks, some additional diffraction peaks were observed at 2θ values of ≈ 35.6 , 38.9 , 48.9 , 53.7 , 58.4 , 61.6 , and 66.4° , which are associated with the (11–1), (111), (20–2), (020), (202), (11–3), and (31–1) crystalline planes of the monoclinic CuO (JCPDS, 48–1548), respectively.⁶⁰ As observed from the diffractograms of NCs, with increasing concentrations of Cu (10–50%), the diffraction peak intensities of CuO gradually increase but conversely decrease in the peak intensities of ZnO. The XRD patterns of the synthesized NCs clearly revealed the presence of ZnO and CuO without any impurities.

The average crystallite sizes of the synthesized ZnO and ZnO/CuO samples were calculated from their highest three diffraction peaks using the Debye–Scherrer's formula (eq 3).⁶¹

$$D = \frac{K\lambda}{\beta \cos \theta} \quad (3)$$

where D : crystallite size (nm), K : Scherrer's constant, (0.9), λ : wavelength of the X-ray source (0.15406 nm), β : peak full

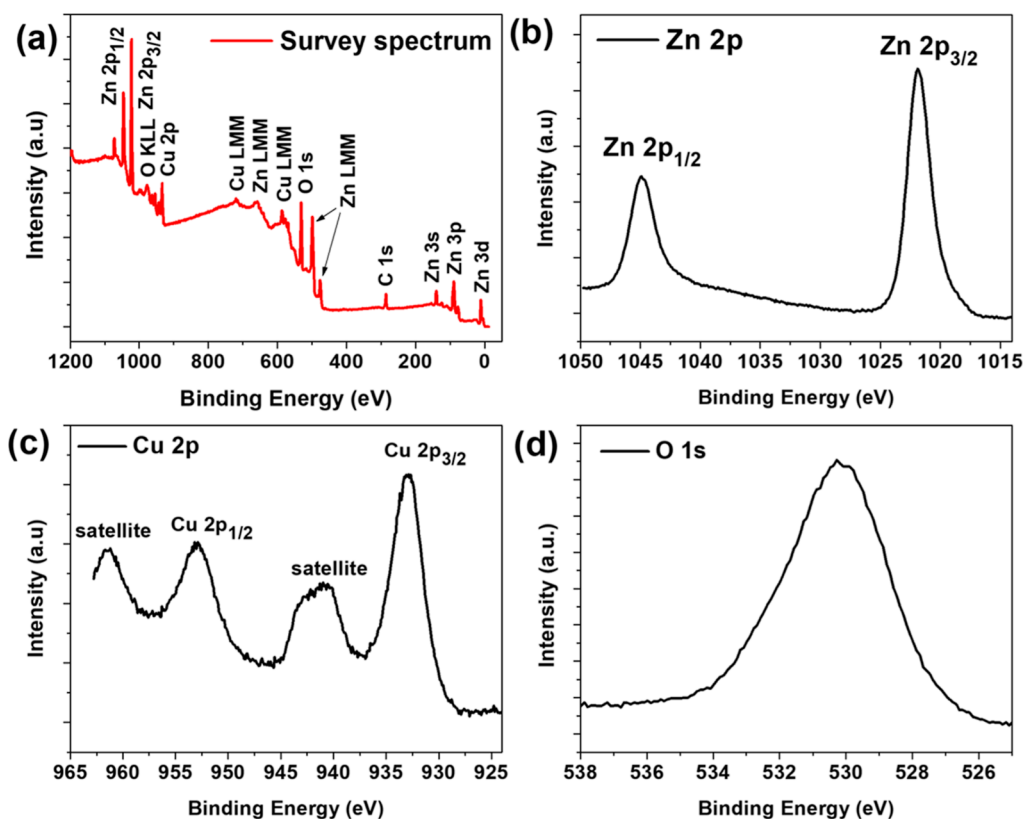


Figure 3. XPS analysis results for the ZC50(ext) sample: (a) full survey scan and (b–d) high resolution spectra for Zn 2p, Cu 2p, and O 1s, respectively.

width at half-maximum intensity (fwhm), and θ : peak position (Bragg's diffraction angle). The calculated average crystal size values for all synthesized samples are presented in Table S1 (in Supporting Information). As seen, the biosynthesized ZnO(ext) sample exhibited a smaller crystallite size as compared to the chemical route synthesized (W–ZnO) sample. Some bioactive capping and stabilizing agents from the leaf extract of *C. macrostachyus*^{51–58} might be responsible for the crystallite size reduction of the ZnO(ext) sample during its synthesis. Similar results were also reported in previous studies for various plant extract-mediated syntheses of metal oxide NPs.^{32–39}

3.2. FTIR Analysis. FT-IR spectroscopy was also used to identify the functional groups of the green-mediated ZnO NPs (ZnO(ext)) and ZnO/CuO NCs (ZC20(ext)) samples, and the resultant spectra in the scanning range of 400–4000 cm^{-1} are depicted in Figure 1b. The FTIR result of the chemically synthesized ZnO NPs (W–ZnO) is also provided for comparison. The spectra of all samples showed a wide peak at $\sim 476 \text{ cm}^{-1}$, which corresponds to the Zn–O bond vibrations.⁴² In the FTIR spectrum of the ZC20(ext) sample along with the peak of Zn–O, the band associated with Cu–O stretching could also be detected at $\sim 684 \text{ cm}^{-1}$ with low intensity owing to its low molar percentage in the sample.⁶² Thus, the spectrum obtained from the ZC20(ext) sample revealed the formation of both oxides in the NC form, which agreed well with the results obtained from other characterizations. The band observed at $\sim 1385 \text{ cm}^{-1}$ in all spectra could be assigned to the stretching of the NO_3^- group resulted from precursors used in synthesis. The broad band in the range of 3200–3500 cm^{-1} corresponds to O–H bond stretching, which might be owing to the surface-adsorbed molecules of water.⁶¹

The FT-IR spectra of biosynthesized samples (ZnO(ext) and ZC20(ext)) display an additional peak around 1628 cm^{-1} , which is not present in the FTIR spectrum of chemically synthesized W–ZnO. This peak could be attributed to stretching vibration of the C=O bond of the organic molecules from plant extract,^{54,57} indicating the presence of some biomolecules in the *C. macrostachyus* leaf after calcination.

3.3. Morphological Analysis. The surface morphologies of the synthesized NPs and NCs were observed using SEM, and the resultant images are displayed in Figure 2a–c and Figure S1 (in Supporting Information). The particle size distribution histogram and the corresponding average particle size for all samples were also obtained by random measuring of 480 particles, and the results are shown in Figure S2 (in Supporting Information). The SEM image of the chemically prepared W–ZnO (Figure 2a) shows the formation of almost spherical and cylindrical NPs with high agglomeration in big clusters. Meanwhile, as observed in Figure 2b, the morphology of biosynthesized ZnO(ext) demonstrates the presence of spherical and triangle-shaped NPs with low agglomeration and a nearly uniform size distribution. Similarly, as can be seen from figures, Figures 2c and S1 (in Supporting Information), the green synthesized NCs also have nearly spherical shapes with an almost uniform and less agglomerated form. However, compared with chemically synthesized W–ZnO, the particle sizes for the green-mediated ZnO(ext), ZC20(ext), and ZC50(ext) samples were decreased (Figure S2), which is in accordance with the XRD findings. The decreasing particle size for green the synthesized sample might be due to the presence of some bioactive functional groups from the leaf extract of *C. macrostachyus*, which can stabilize and cap the particles and

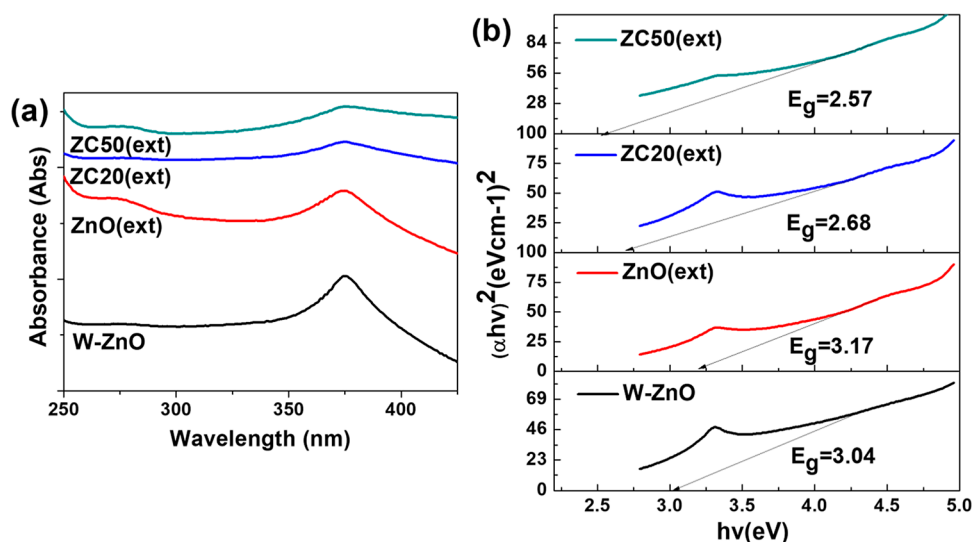


Figure 4. (a) UV–visible optical absorbance and (b) corresponding Tauc's plots of W–ZnO, ZnO(ext), ZC20(ext), and ZC50(ext) samples.

also prevent their agglomeration during the synthesis process.^{32,33}

The elemental constitution of ZC50(ext) was also analyzed using the EDX system on the same SEM, and the results are displayed in Figure S3 (in Supporting Information) and Figure 2d. EDX spectrum for the ZC50(ext) sample (Figure S3) revealed the existence of zinc, copper, and oxygen elements without any other impurities. The weight percentages of Zn, Cu, and O in ZC50(ext) NC sample were determined to be 41.09, 44.61, and 14.30%, respectively. Figure 2d illustrates the distribution of Zn, Cu, and O, respectively. This indicates that Zn, Cu, and O elements are distributed uniformly, confirming that CuO and ZnO are well-distributed in the NC, which will be favorable for photocatalytic application.

The exact morphology, particle size, and crystallinity of the biosynthesized ZC50(ext) sample were also further analyzed using TEM. The low-resolution TEM micrographs of ZC50(ext) (Figure 2e,f) display spherical and polygonal morphologies, with particle sizes ranging from 17 to 52 nm. The HR-TEM image of ZC50(ext) NC (Figure 2g) clearly demonstrates the formation of the heterojunction between intimately contacted CuO and ZnO. From Figure 2g, the two measured fringe spacings of 0.28 and 0.247 nm match well with the values of (100) and (101) crystal planes of ZnO, respectively, with a hexagonal wurtzite structure. On the other hand, the lattice fringes observed with interplanar distance of 0.251 nm are associated with the (11–1) crystal plane of monoclinic CuO. Figure 2h is the fast Fourier transform (FFT) pattern of Figure 2g, which further determined the crystal lattice planes of ZnO and CuO. The clear lattice fringes observed on both oxides also confirm their highly crystalline nature.

3.4. XPS Analysis. XPS analysis was conducted to probe the composition and oxidation states of the surface elements present in the green synthesized ZnO/CuO NC (ZC50(ext)) sample, and the resultant XPS spectra are displayed in Figure 3. The C 1s peak (at 284.8 eV) was used as a reference to calibrate the binding energy values in these spectra. The full scan XPS spectrum (Figure 3a) verified that the surface of the ZC50(ext) sample was merely composed of Zn, Cu, and O without any other impurities. Figure 3b presents the Zn 2p XPS spectrum with high resolution, in which two strong peaks appeared at 1021.88 and 1044.88 eV, corresponding to Zn

2p_{3/2} and Zn 2p_{1/2} levels, respectively. The binding energy difference between the two levels is around 23.0 eV, which confirms the +2 oxidation state of Zn in the ZC50(ext) sample.¹⁶ Figure 3c gives the Cu 2p high-resolution XPS spectrum with two dominant peaks located at 933.1 and 953.2 eV corresponding to Cu 2p_{3/2} and Cu 2p_{1/2} levels, respectively. The two other peaks with satellite features centered at 942.1 and 961.7 eV also indicate the existence of Cu in a bivalence oxidation state.¹⁸ In the O 1s XPS spectrum (Figure 3d), the peak that appeared at 530.16 eV can be related to the lattice oxygen that bonded with metals in O₂[−] ion form.¹⁸ Overall, the above XPS results manifest the presence of ZnO and CuO in the synthesized ZC50(ext) sample, which is in concordance with the XRD, EDS, and HR-TEM findings.

3.5. UV–Vis Spectral Analysis. The optical absorption properties of the prepared W–ZnO, ZnO(ext), ZC20(ext), and ZC50(ext) samples were also investigated through UV–visible spectroscopy analysis, and the resulting spectra are displayed in Figure 4a. The spectra of all samples exhibited an intensive absorption around 375 nm which could be ascribed to the characteristic absorbance band of ZnO due to its intrinsic band gap transitions (O_{2p}–Zn_{3d}).³⁹ The absorbance of the chemically synthesized W–ZnO sample is limited in the UV region, while the green synthesized ZnO(ext) showed broad absorption that extended to the visible region due to the presence of some functional groups from the extract. However, the ZnO(ext) peak in its UV region displayed a slight blue shift as compared to the W–ZnO band, which may be related to the quantum confinement effect resulted from particle size reduction in the ZnO(ext) sample.⁴² On the other hand, compared to pristine ZnO NPs, the ZC20(ext) and ZC50(ext) NC samples exhibited a broad range of absorption that significantly extended toward the visible light region. The observed spectral response broadening by the addition of CuO could be related to the formation of additional states due to interfacial interaction between conjugated metal oxides, and this results in a remarkable red shift in the absorption edge of the resulting NCs. In addition, the visible light response of the NCs also the increased with increasing content of CuO.

Further, the optical band gap for each of the synthesized samples was also estimated using the following Tauc's relation⁶³

$$(\alpha h\nu) = A(h\nu - E_g)^{n/2} \quad (4)$$

where ν = incident photon frequency, h = Planck's constant, α = the coefficient of absorption, A = proportional constant, n = the power index referring to the nature of the transition, and its value for direct transitions is 1.^{63,64} By extrapolating the linear region of $(\alpha h\nu)^2$ versus the $h\nu$ axis, as illustrated in Figure 4b, direct band gaps can be estimated. In this work, the band gap values of W–ZnO, ZnO(ext), ZC20(ext), and ZC50(ext) samples were estimated to be about 3.04, 3.17, 2.68, and 2.57 eV, respectively. As observed, the band gap values of the synthesized NCs were all lower than those of pristine ZnO samples, which also affirms the formation of NC, as explained above. On the other hand, compared with chemically synthesized W–ZnO, the band gap value obtained for green-mediated ZnO(ext) is increased, owing to the quantum size effect.

3.6. Photoluminescence Analysis. The room-temperature photoluminescence (PL) analysis was conducted to determine the charge carrier separation and recombination efficiency of the prepared W–ZnO, ZnO(ext), ZC20(ext), and ZC50(ext) samples, and the resultant PL spectra at an excitation wavelength of 325 nm are depicted in Figure 5.

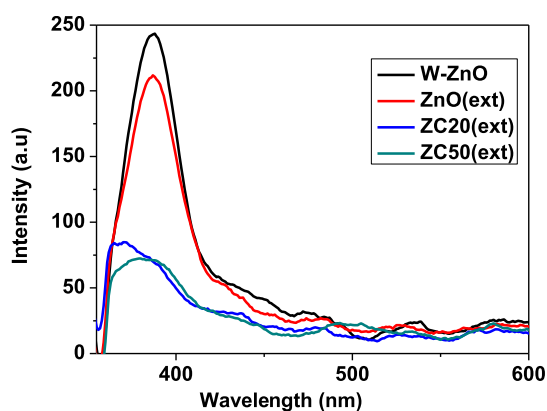


Figure 5. PL spectra of W–ZnO, ZnO(ext), ZC20(ext), and ZC50(ext) samples.

All the samples show a strong UV emission band around 387 nm and relatively weaker visible emission peaks around 438, 451, 472, and 532 nm. The intense UV emission peak appeared at 387 nm, ascribed to the near band-edge emission of ZnO originated from the recombination of excitons,²² whereas emission bands observed in the visible range could be related to various defect-mediated recombination of charge. As seen, the UV emission intensities from ZnO/CuO NCs samples are much lower than those of pristine ZnO samples, indicating a reduced recombination rate of photoexcited e^-/h^+ pairs in ZnO/CuO NCs. This implies that the coupling of ZnO with CuO promotes the interfacial charge carrier transfer between the two metal oxides, which can greatly suppress the direct recombination of excitons and hence prolong charge carrier lifetime. Thus, the efficient charge carrier separation due to the formation of heterojunction between ZnO and CuO is favorable for enhancing the photocatalytic activity of the resulting NC. On the other hand, compared with chemically synthesized W–ZnO, the green-mediated ZnO(ext) NPs showed relatively lower PL intensity around 387 nm, which may be due to the presence of nonradiative quenching

originated from surface impurities and defects in the biosynthesized ZnO NPs.

3.7. Electrochemical Analysis. Mott–Schottky (M–S) analyses were conducted to determine the band potentials of the synthesized materials, and Figure S4a,b (in Supporting Information) depicts the M–S plots for ZnO(ext) NPs and ZC20(ext) NCs, respectively. The M–S curve of ZnO(ext) exhibited a positive slope (n-type character) with a flat band potential (E_{fb}) of -0.4 V (vs Ag/AgCl). However, the curve of ZC20(ext) showed both positive (n-type character) and negative (p-type character) slopes with E_{fb} values of -0.32 and 1.3 V (vs Ag/AgCl), respectively, confirming the formation of the p–n heterojunction between ZnO and CuO.²² The measured potentials (vs Ag/AgCl) and the corresponding values relative to the reversible hydrogen electrode are given in Table S2. According to the literature, the conduction band (CB) edge of n-type semiconductors is more negative than the flat-band potential (E_{fb}) by ~ 0.1 V, while the valence band (VB) edge of p-type semiconductors is more positive than the (E_{fb}) by ~ 0.1 V.⁶⁵ Thus, the CB potential (E_{CB}) of n-type semiconductors and the VB potential (E_{VB}) of p-type semiconductors can be estimated from their E_{fb} values, while the corresponding VB and CB potentials of n-type and p-type semiconductors can be calculated using eq 5.⁶⁵

$$E_{VB} = E_{CB} + E_g \quad (5)$$

where E_g is bandgap energy obtained from Tauc's formula. Thus, the E_{CB} and E_{VB} values of ZnO(ext) NPs are 0.1 and 3.28 V, respectively. In ZC20(ext) NCs, the E_{CB} and E_{VB} values of ZnO and CuO were found to be 0.19 and 2.87 V for ZnO and -0.67 and 2.01 V for CuO, respectively.

3.8. Photocatalytic Activity. The photoreactor and time-dependent decolorization of the MB dye solution under visible light irradiation with ZC50(ext) NCs are presented in Figure S5. The photodegradation performance of the synthesized NPs and NCs samples was evaluated against MB dye under 80 min of visible light irradiation. Figure 6a–e displays the time-dependent absorption spectra showing the photodegradation of MB dye using W–ZnO, ZnO(ext), ZC10(ext), ZC20(ext), and ZC50(ext) samples as photocatalysts. As observed in all spectra, the absorption peak of MB decreased gradually with an increase of the exposure time for all synthesized samples. However, a more remarkable change in MB absorbance was noticed for NC samples than for pure ZnO NPs. The MB degradation percentage was calculated using eq 1, and the graph of percent degradation vs illumination time for all samples is presented in Figure 6f. After 80 min of visible light exposure, about 74.13, 77.73, 90.02, 97.02, and 95.03% of MB were degraded by the samples W–ZnO, ZnO(ext), ZC10(ext), ZC20(ext), and ZC50(ext), respectively. As seen, the photodegradation efficiency of the biosynthesized ZnO(ext) sample was higher than that of the chemically synthesized W–ZnO sample. This enhancement might be related to the improved surface charge and smaller particle size of green-mediated ZnO.³² As can be seen from SEM and XRD results, the particle size of the ZnO(ext) sample was smaller than that of W–ZnO. As mentioned before, some bioactive metabolites of the plant extract could be responsible for the size reduction and stabilization of the green-mediated ZnO NPs. Thus, smaller particle sizes of ZnO(ext) NPs provide larger surface area, which is more favorable for enhanced photodegradation of MB dye. Furthermore, as observed from the FTIR analysis, the biosynthesized samples have negative/positive charges on their

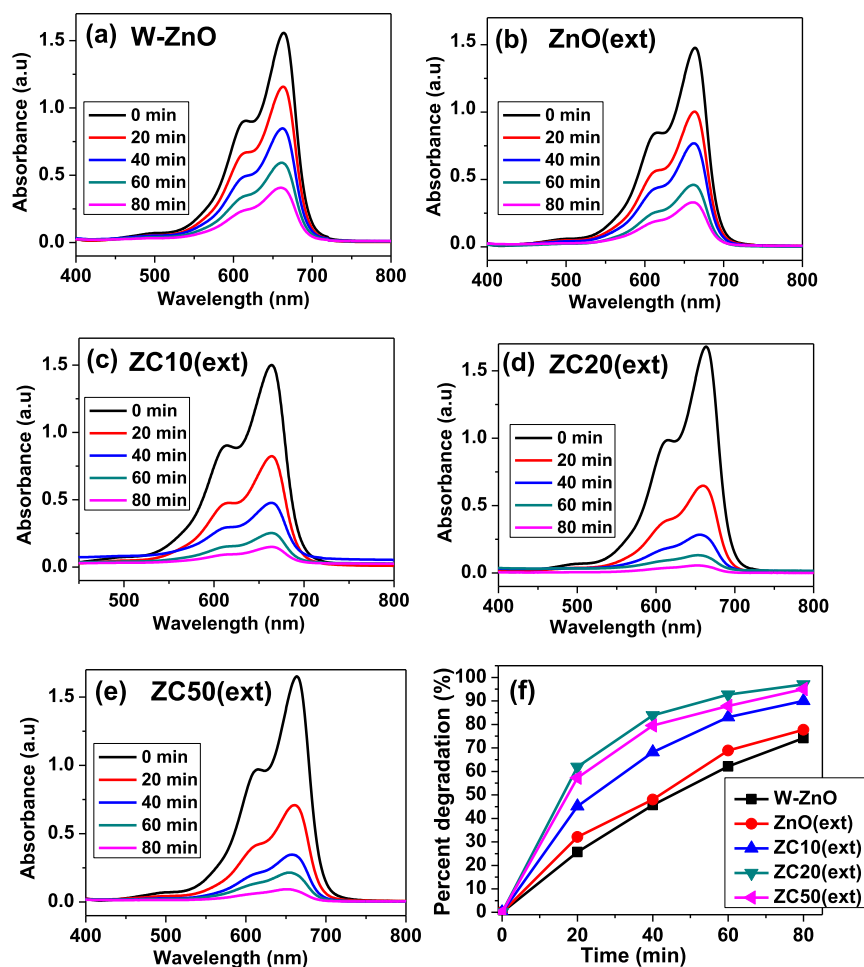


Figure 6. (a–e) UV–Vis spectra depicting the photodegradation of MB dye and (f) the corresponding photodegradation efficiency in the presence of W–ZnO, ZnO(ext), ZC10(ext), ZC20(ext), and ZC50(ext) samples under visible light irradiation.

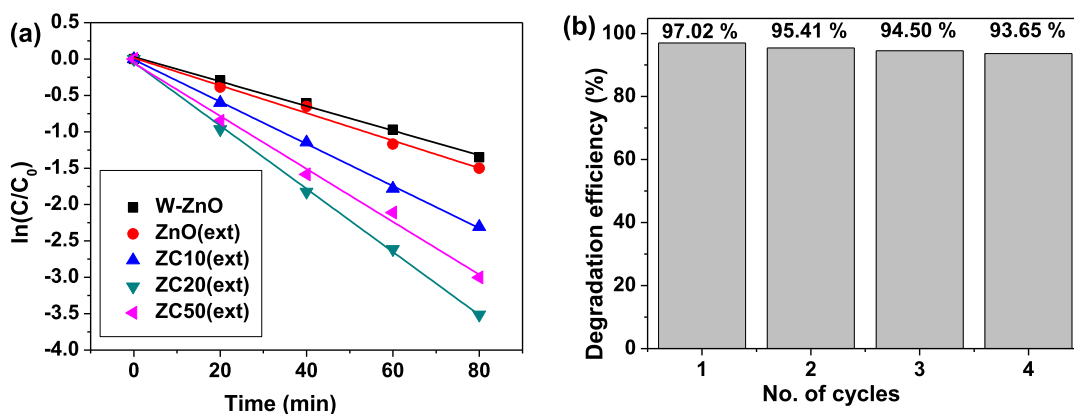


Figure 7. (a) Plots of $\ln(C/C_0)$ vs time for the photodegradation of the MB dye using W–ZnO, ZnO(ext), ZC10(ext), ZC20(ext), and ZC50(ext) samples under visible light irradiation and (b) reusability of the ZC20(ext) sample for four consecutive runs.

surface due to the surface-adsorbed biomolecules of the plant extract. The presence of these charges on the photocatalyst surface could be helpful to facilitate its interaction with cationic MB dye, which in turn leads to enhanced photocatalytic activity.

On the other hand, it is obvious that all of the synthesized ZnO/CuO NCs exhibited highly improved visible light-driven photocatalytic activities compared to those of ZnO NPs. The observed higher photodegrading efficiencies of the binary NCs

might be ascribed to the formation of the heterojunction between the two metal oxides, which can markedly suppress the recombination of photogenerated charge carriers and boost the photoresponsive range in the visible region.^{16,19} Further, it was also observed that the ratio of the CuO component has a considerable effect on the photocatalytic efficiency of the resulting NC. As demonstrated in Figure 6f, the photocatalytic activity of the ZnO/CuO NCs increases with increasing the CuO content from 10 to 20 mol %. However, any further

incorporation of CuO above 20 mol % led to a reduction in the photodegradation efficiency of the NC because the excessive CuO content could be another recombination center for photogenerated charge carriers, and it can also shade the active sites of ZnO from incident light. Among all samples, the ZnO/CuO NC prepared with 20 mol % of the Cu precursor (ZC20(ext)) showed the highest photocatalytic performance.

The photodegradation kinetics was also investigated, and as shown in Figure 7a, the degradation processes of MB for all prepared samples are well fitted with pseudo-first-order eq (eq 2). From the graph of $\ln(C/C_0)$ vs time, the first order rate constant values were determined to be 0.01689, 0.01893, 0.02896, 0.04338, and 0.03632 min^{-1} , for W–ZnO, ZnO(ext), ZC10(ext), ZC20(ext), and ZC50(ext) samples, respectively. As seen from the kinetics results, the NC samples showed remarkably improved photocatalytic degradation rates compared to those of the ZnO samples. In particular, ZC20(ext) exhibited a superior rate for degradation of MB dye, which is about 2.6 times faster than pure ZnO. Compared with the chemically synthesized W–ZnO sample, the photodegradation rate for the biosynthesized ZnO(ext) sample increased. This indicates the beneficial effects of the employed extract for the preparation of a better catalyst with enhanced surface area. The calculated rate constants (k), R^2 values, and degradation efficiency (%) after 80 min of irradiation for all of the prepared samples are summarized in Table 1. The photostability and

Table 1. Observed Values of Rate Constants (k), Regression Coefficient (R^2), and Degradation Efficiency for the Synthesized Samples

sample	K (min^{-1})	R^2	percent degradation (%) after 80 min of irradiation
W–ZnO	0.01689	0.99599	74.13
ZnO(ext)	0.01893	0.98997	77.73
ZC10(ext)	0.02896	0.99913	90.02
ZC20(ext)	0.04338	0.9986	97.02
ZC50(ext)	0.03632	0.99223	95.03

reusability of ZC20(ext) NCs were also examined for four cycles of photodegradation of MB dye under irradiation of visible light. After each run, the photocatalyst was separated from the solution by centrifugation and reused again for subsequent runs with the freshly prepared MB solution. As shown in Figure 7b, the photodegradation efficiency of ZC20(ext) was not significantly changed even after four consecutive cycles, which indicates the appreciable stability and durability of the prepared photocatalyst.

Table 2 compares the photocatalytic performance of our synthesized ZnO/CuO NCs with previously reported ZnO/CuO and other ZnO-based NCs toward MB degradation. It is obvious that the ZnO/CuO NCs obtained in this work exhibited significantly improved photocatalytic performance compared to that of other ZnO-based photocatalysts, which clearly affirms the efficiency of our green-mediated ZnO/CuO NCs as a better photocatalyst. The observed higher photocatalytic activity of our catalyst could be ascribed to the formation of smaller particles with a larger surface area, which may result from the strong capping and stabilizing capacity of the plant extract used during the synthesis.

3.9. Photocatalytic Activity by COMSOL Simulation.

To validate and predict the experimental results, the theoretical photocatalytic activity of ZnO/CuO NCs based on experimental conditions was also simulated via mathematical modeling based on FEM using COMSOL Multiphysics. The FEM-based mathematical modeling approach allows for a comprehensive analysis of the ZnO and CuO NCs behavior when exposed to EM waves. By employing the RF and wave optics and time-dependent module in COMSOL software (version 6.1a), the theoretical 3D model can be accurately simulated. This simulation is based on the built-in Maxwell equations (eqs 6–8), which describe the propagation and interaction of EM waves with the NC structure. Using this model, the absorption of EM waves within the same wavelength range as the experimental setup can be deeply investigated.

$$\nabla \times \mu_r^{-1}(\nabla \times E) - k_0^2 \left(\epsilon_r - \frac{j\sigma}{\omega\epsilon_0} \right) E = 0 \quad (6)$$

$$(\nabla - ik_1) \times \mu_r^{-1}((\nabla - ik_1) \times E1) - k_0^2 \left(\epsilon_r - \frac{i\sigma}{\omega\epsilon_0} \right) E1 = 0 \quad (7)$$

$$(\nabla - ik_2) \times \mu_r^{-1}((\nabla - ik_2) \times E2) - k_0^2 \left(\epsilon_r - \frac{i\sigma}{\omega\epsilon_0} \right) E2 = 0 \quad (8)$$

As shown in Figure 8, the 3D model built for this study is based on three different kinds of boundaries, which are termed periodic boundary conditions, scattered boundary conditions, primary boundary conditions, and the perfectly matched layers (PML) condition at the back of the internal continuity boundaries. This built-in model is used to simulate the photodegradation of MB by ZnO/CuO NCs with EM waves as

Table 2. Comparison of the Photocatalytic Degradation of MB by Various ZnO/CuO and Other ZnO-Based NCs

catalyst	synthesis method	experimental conditions				performance		
		catalyst (mg)	conc. of MB (ppm)	light	time (min)	rate const. k (min^{-1})	degradation (%)	refs
CuO–ZnO	green	20	20 ppm	vis	105	0.017	82	22
CuO–ZnO	green	25	10^{-3} M	vis	120	0.0235	95.6	66
ZnO/CuO	combustion	40	20 ppm	solar	60	0.0223	93	67
ZnO/CuO	hydrothermal	50	5 ppm	Solar	180	0.0033	46	68
CuO–ZnO	reflux condensation	50	15 ppm	UV	120	0.01948	93.66	69
Cr ₂ O ₃ /ZnO	green	25	10 ppm	vis	90	0.08	85	70
ZnO/Fe ₃ O ₄	hydrothermal	50	5 ppm	solar	180	0.0078	76	68
CoO/ZnO	precipitation	100	7 ppm	UV	180	0.00643	67.5	71
ZnO/CuO	green	30	10 ppm	vis	80	0.04338	97.02	this work

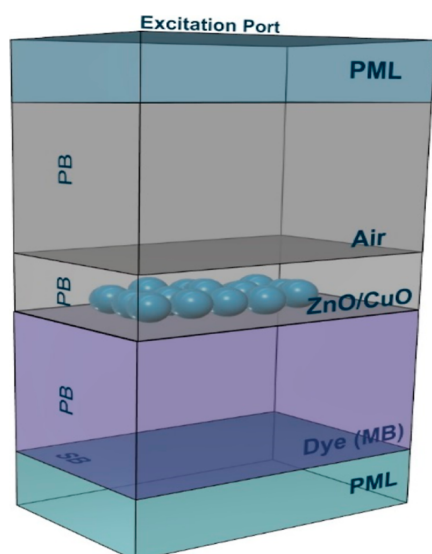


Figure 8. Schematic diagram of the 3D COMSOL simulation model.

incident light (wavelength: 250–500 nm). Here, ZnO/CuO NCs are set to be spherical particles of 30 nm diameter, and the refractive index of MB, water, and air is 1.347, 1.33, and 1.00, respectively. During the photocatalytic simulation, EM wave outcomes were obtained at regular time intervals ranging from 0 to 80 min, according to experimental values. The 3D contours of concentration change showing the photodegradation of MB by ZnO/CuO NCs (with 20 mol % of CuO) are shown in Figure 9. As displayed in this figure, with increasing

time of exposure, the highest concentration region (red area) is reduced, while the lowest concentration part (blue area) is increased, indicating a gradual decrease in the concentration of MB. The simulation result indicated that the degradation efficiency reaches 98% within 80 min, which is very close to the value obtained experimentally (97.02%) by the ZC20(ext) NCs sample.

Further, the kinetics for photodegradation of MB dye in the presence of ZnO/CuO (20%) NCs were also studied theoretically using the above-built mathematical model, and the first-order rate constant value obtained via simulation is 0.03379 min^{-1} . Figure 10 compares the experimental and

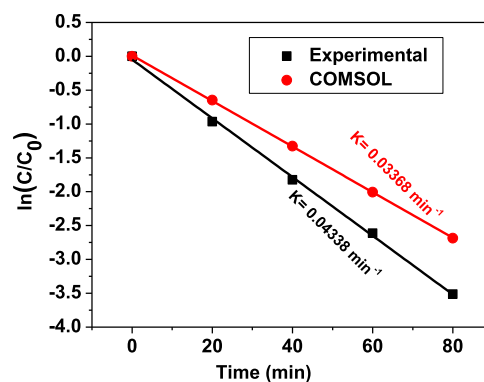


Figure 10. Experimental and simulation plots of $\ln(C/C_0)$ vs time for the photodegradation of MB dye using ZnO/CuO (20%) NCs.

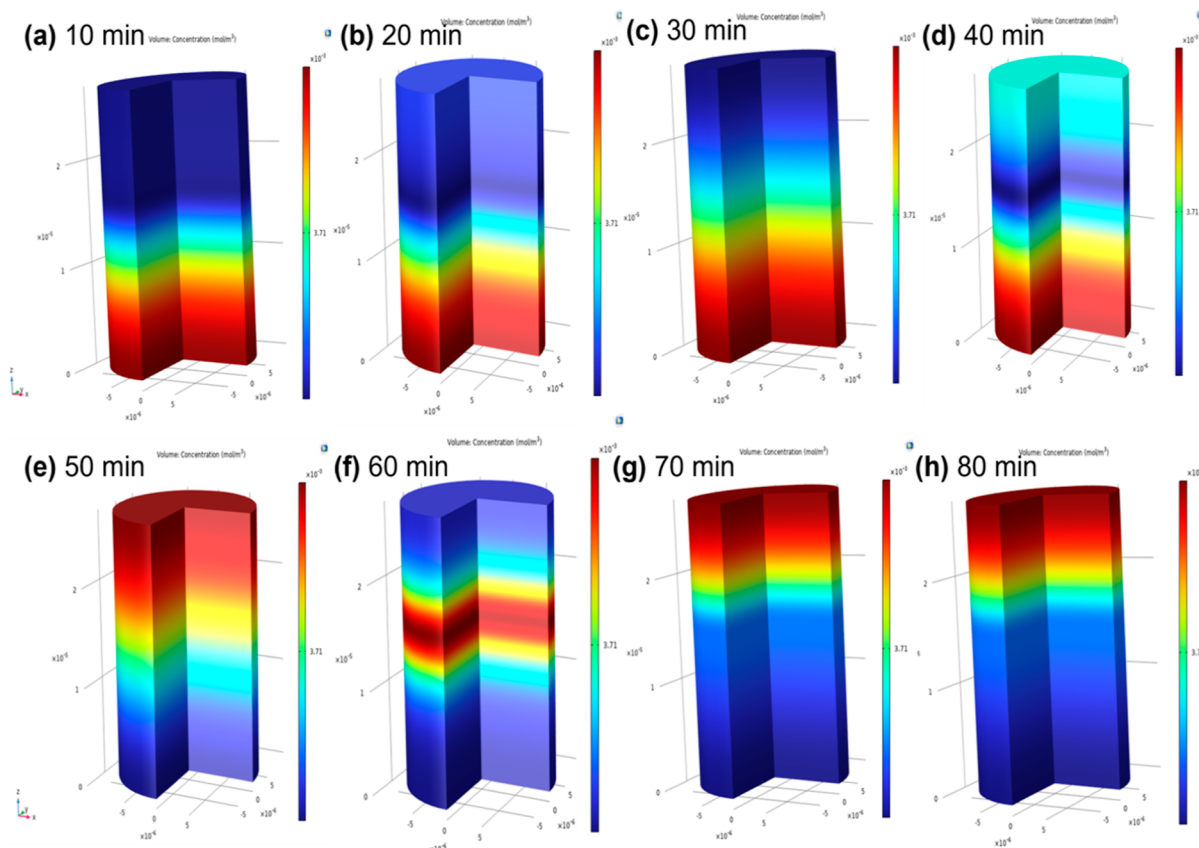


Figure 9. 3D contours of the concentration change of MB by ZnO/CuO (20%) NCs.

theoretically obtained photodegradation rates of MB by ZnO/CuO (20%) NCs. As reported in previous sections, the experimentally obtained rate constant value for the ZC20(ext) NCs sample was 0.04338 min^{-1} . The observed rate constant difference between experimental and simulation results may possibly be due to the fact that simulation is carried out by considering a rigid and regular spherical geometry instead of irregular spheres of ZnO/CuO NC formed experimentally. This discrepancy in geometry could lead to differences in the surface area and active sites available for the photodegradation process. Moreover, the modified surface charge of the green-mediated ZC20(ext) NCs sample due to some surface-adsorbed functional groups of the plant extract has not been considered during simulation, which may also be another reason for the difference in degradation rate results.

Based on the experimental and theoretical results, a possible photoinduced degradation mechanism of MB by ZnO/CuO NCs was also proposed and represented schematically, as shown in Figure 11. As observed from the Mott–Schottky

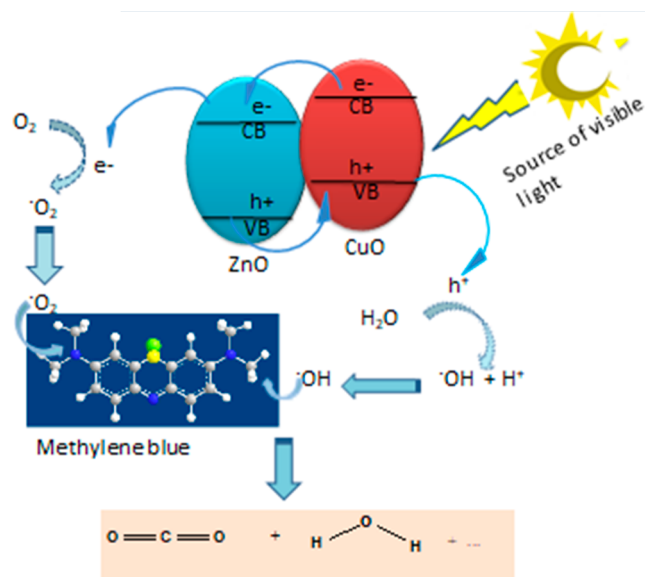
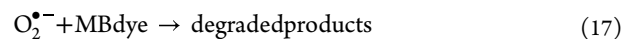
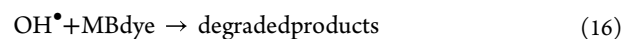
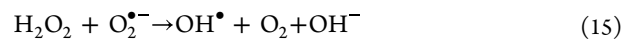
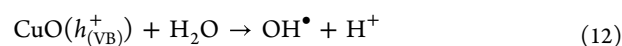
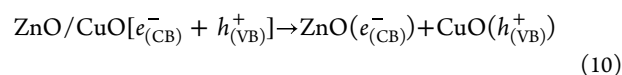
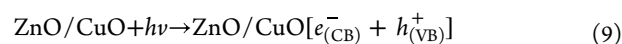


Figure 11. Schematic photoinduced dye degradation mechanism of ZnO/CuO NCs under visible light.

analysis, the M-S curve of the prepared NC revealed the coexistence of p- and n-type characters, confirming the formation of p–n heterojunction in ZnO/CuO NCs. A significantly reduced PL emission observed from the NC samples also confirms the efficient charge carrier separation due to the formation of the p–n heterojunction between ZnO and CuO. The coupling of ZnO as the n-type semiconductor with p-type CuO to produce the p–n heterojunction assists in the separation of photoexcited charge carriers by inducing an electric field at the contact interface of the two metal oxides. Upon absorption of visible light, electrons from both semiconductors are excited from their VB to CB, leaving behind holes in their VB. Since both the CB and VB levels of ZnO lie below those of CuO, thermodynamically favorable transfer of the photoinduced electrons occurs from the CB of CuO to the CB of ZnO, whereas the holes in the VB of ZnO are transferred to that of CuO. In this way, the recombination rate of the photogenerated e^-/h^+ pairs is significantly reduced, and their lifetime is prolonged until they reach the photo-

catalyst surfaces. Then, photoexcited electrons react with molecular oxygen to produce superoxide anion radicals ($\text{O}_2^{\bullet-}$), while the photogenerated holes are trapped by water molecules and hydroxide ions to generate hydroxyl radicals ($\bullet\text{OH}$). The generated highly reactive radicals readily oxidize and degrade dye molecules. The main reactions involved in the photodegradation process can be described by the following equations⁶⁸



4. CONCLUSIONS

The potential application of *C. macrostachyus* leaf extracts as natural stabilizing as well as reducing agents for the biofabrication of nanostructured materials is explored for the first time. The present green method was successful in producing highly pure ZnO and ZnO/CuO nanostructures in a rapid, environmentally benign, and cost-effective way. For comparison purposes, pure ZnO NPs were also synthesized without using plant extract. Many characterization techniques have been exploited to probe the various properties of the synthesized samples, and all of the obtained results apparently confirmed the formation of ZnO NPs and ZnO/CuO NCs. SEM studies also revealed the formation of almost spherical-shaped particles in all samples, but the average particle sizes of the biosynthesized samples decreased. The prepared ZnO/CuO NCs demonstrated substantially strong absorption in both UV and visible regions. For visible light-driven photodegradation of MB dye, these NCs exhibited a remarkably enhanced photocatalytic performance compared that of bare ZnO NPs. In particular, for optimized ZnO/CuO NC, about 97% MB degradation was achieved after 80 min of visible light irradiation. In addition, the prepared NCs exhibited appreciable photocatalytic stability and reusability without significant change in their activity after four consecutive runs. Furthermore, the photocatalytic performance of ZnO/CuO NCs was also successfully predicted by 3D COMSOL simulation. The simulation and the experimental results showed good agreement with a minor distinction. Thus, the present green-mediated ZnO/CuO NC can be a promising visible-light-active photocatalyst for the removal of organic pollutants from wastewater. Furthermore, due to its promising physicochemical, optical, and electrical properties, the prepared NC is also expected to have a potential application in antibacterial and sensor fields.

■ ASSOCIATED CONTENT

SI Supporting Information

The Supporting Information is available free of charge at <https://pubs.acs.org/doi/10.1021/acsomega.3c06155>.

Average crystalline sizes of NCs and nanomaterials; schematic representation of synthesis routes of the nanomaterials; SEM image of ZC20(ext) samples; particle size distribution; EDX spectrum of ZC50(ext) samples; and Mott-shottky plots of ZnO NPs and ZC20(ext) NCs vs Ag/AgCl (PDF)

■ AUTHOR INFORMATION

Corresponding Authors

Fedlu Kedir Sabir – Department of Applied Chemistry, School of Natural Science, Adama Science and Technology University, Adama, Ethiopia; orcid.org/0000-0002-6235-1530; Email: fedluked130@gmail.com

H. C. Ananda Murthy – Department of Applied Chemistry, School of Natural Science, Adama Science and Technology University, Adama, Ethiopia; Department of Prosthodontics, Saveetha Dental College & Hospital, Saveetha Institute of Medical and Technical Science (SIMATS), Saveetha University, Chennai 600077 Tamil Nadu, India; orcid.org/0000-0002-2361-086X; Email: anandkps350@gmail.com

Authors

Solomon Bekele Endeshaw – Department of Applied Chemistry, School of Natural Science, Adama Science and Technology University, Adama, Ethiopia

Lemma Teshome Tufa – Department of Applied Chemistry, School of Natural Science, Adama Science and Technology University, Adama, Ethiopia; Research Institute of Materials Chemistry, Chungnam National University, Daejeon 34134, Republic of Korea; orcid.org/0000-0001-6929-8464

Mahendra Goddati – Department of Physics, Chungnam National University, Daejeon 34134, Republic of Korea

Jaebom Lee – Department of Chemistry, Chemistry Engineering and Applied Chemistry, Chungnam National University, Daejeon 34134, Republic of Korea; orcid.org/0000-0002-8414-7290

Vanna Christmas Silalahi – Department of Physics, Chungnam National University, Daejeon 34134, Republic of Korea; orcid.org/0000-0003-4660-4195

Donghan Lee – Department of Physics, Chungnam National University, Daejeon 34134, Republic of Korea

Complete contact information is available at: <https://pubs.acs.org/doi/10.1021/acsomega.3c06155>

Notes

The authors declare no competing financial interest.

■ ACKNOWLEDGMENTS

The authors would like to thank Adama Science and Technology University for financial and research materials/equipment support. This research was also partly supported by the Industrial Strategic Technology Development Program, grant number 20025720, funded by the Ministry of Trade, Industry & Energy (MOTIE, Korea). This research was also partly supported by “Regional Innovation Strategy (RIS)” through the National Research Foundation of Korea (NRF)

funded by the Ministry of Education (MOE) (2021RIS-004), project number 1345370812.

■ REFERENCES

- (1) Carmen, Z.; Daniel, S. Textile Organic Dyes - Characteristics, Polluting Effects and Separation/Elimination Procedures from Industrial Effluents - A Critical Overview. *Organic Pollutants Ten Years After the Stockholm Convention—Environmental and Analytical Update*; Tech, 2012, pp 55–86.
- (2) Ilyas, M.; Ahmad, W.; Khan, H.; Yousaf, S.; Yasir, M.; Khan, A. Environmental and Health Impacts of Industrial Wastewater Effluents in Pakistan: A Review. *Rev. Environ. Health* **2019**, *34*, 171–186.
- (3) Ibrahim, R. K.; Hayyan, M.; AlSaadi, M. A.; Hayyan, A.; Ibrahim, S. Environmental Application of Nanotechnology: Air, Soil, and Water. *Environ. Sci. Pollut. Res.* **2016**, *23*, 13754–13788.
- (4) Ahmed, S. N.; Haider, W. Heterogeneous photocatalysis and its potential applications in water and wastewater treatment: a review. *Nanotechnology* **2018**, *29*, 342001.
- (5) Byrne, C.; Subramanian, G.; Pillai, S. C. Recent advances in photocatalysis for environmental applications. *J. Environ. Chem. Eng.* **2018**, *6*, 3531–3555.
- (6) Karthikeyan, C.; Arunachalam, P.; Ramachandran, K.; Al-Mayouf, A. M.; Karuppachamy, S. Recent advances in semiconductor metal oxides with enhanced methods for solar photocatalytic applications. *J. Alloys Compd.* **2020**, *828*, 154281.
- (7) You, J.; Guo, Y.; Guo, R.; Liu, X. A review of visible light-active photocatalysts for water disinfection: Features and prospects. *Chem. Eng. J.* **2019**, *373*, 624–641.
- (8) Velempini, T.; Prabakaran, E.; Pillay, K. Recent Developments in the Use of Metal Oxides for Photocatalytic Degradation of Pharmaceutical Pollutants in Water—a Review. *Mater. Today Chem.* **2021**, *19*, 100380.
- (9) Rajamanickam, D.; Shanthi, M. Photocatalytic degradation of an organic pollutant by zinc oxide - solar process. *Arab. J. Chem.* **2016**, *9*, S1858–S1868.
- (10) Ong, C. B.; Ng, L. Y.; Mohammad, A. W. A Review of ZnO Nanoparticles as Solar Photocatalysts: Synthesis, Mechanisms and Applications. *Renew. Sustain. Energy Rev.* **2018**, *81*, 536–551.
- (11) Pirhashemi, M.; Habibi-Yangjeh, A.; Rahim Pouran, S. Review on the Criteria Anticipated for the Fabrication of Highly Efficient ZnO-based Visible-light-driven Photocatalysts. *J. Ind. Eng. Chem.* **2018**, *62*, 1–25.
- (12) Serrà, A.; Gómez, E.; Philippe, L. Bioinspired ZnO-based solar photocatalysts for the efficient decontamination of persistent organic pollutants and hexavalent chromium in wastewater. *Catalysts* **2019**, *9*, 974.
- (13) Qi, K.; Cheng, B.; Yu, J.; Ho, W. Review on the improvement of the photocatalytic and antibacterial activities of ZnO. *J. Alloys Compd.* **2017**, *727*, 792–820.
- (14) Das, S.; Srivastava, V. C. An overview of the synthesis of CuO-ZnO nanocomposite for environmental and other applications. *Nanotechnol. Rev.* **2018**, *7*, 267–282.
- (15) Saravanan, R.; Karthikeyan, S.; Gupta, V. K.; Sekaran, G.; Narayanan, V.; Stephen, A. Enhanced photocatalytic activity of ZnO/CuO nanocomposite for the degradation of textile dye on visible light illumination. *Mater. Sci. Eng., C* **2013**, *33*, 91–98.
- (16) Xu, L.; Zhou, Y.; Wu, Z.; Zheng, G.; He, J.; Zhou, Y. Improved photocatalytic activity of nanocrystalline ZnO by coupling with CuO. *J. Phys. Chem. Solids* **2017**, *106*, 29–36.
- (17) Sahu, K.; Bisht, A.; Kuriakose, S.; Mohapatra, S. Two Dimensional CuO-ZnO Nanohybrids with Enhanced Photocatalytic Performance for Removal of Pollutants. *J. Phys. Chem. Solids* **2020**, *137*, 109223.
- (18) Chen, C.; Liu, X.; Fang, Q.; Chen, X.; Liu, T.; Zhang, M. Self-assembly synthesis of CuO/ZnO hollow microspheres and their photocatalytic performance under natural sunlight. *Vacuum* **2020**, *174*, 109198.
- (19) Harish, S.; Archana, J.; Sabarinathan, M.; Navaneethan, M.; Nisha, K. D.; Ponnusamy, S.; Muthamizchelvan, C.; Ikeda, H.;

- Aswal, D. K.; Hayakawa, Y. Controlled structural and compositional characteristic of visible light active ZnO/CuO photocatalyst for the degradation of organic pollutant. *Appl. Surf. Sci.* **2017**, *418*, 103–112.
- (20) Sandhya, J.; Kalaiselvam, S. UV Responsive Quercetin Derived and Functionalized CuO/ZnO Nanocomposite in Ameliorating Photocatalytic Degradation of Rhodamine B Dye and Enhanced Biocidal Activity against Selected Pathogenic Strains. *J. Environ. Sci. Health, Part A* **2021**, *56*, 835–848.
- (21) Maru, M. T.; Gonfa, B. A.; Zelekew, O. A.; Fakrudeen, S. P.; Ananda Murthy, H. C.; Bekele, E. T.; Sabir, F. K. Effect of *Musa acuminata* peel extract on synthesis of ZnO/CuO nanocomposites for photocatalytic degradation of methylene blue. *Green Chem. Lett. Rev.* **2023**, *16* (1), 2232383.
- (22) Bekru, A. G.; Tufa, L. T.; Zelekew, O. A.; Goddati, M.; Lee, J.; Sabir, F. K. Green Synthesis of a CuO-ZnO Nanocomposite for Efficient Photodegradation of Methylene Blue and Reduction of 4-Nitrophenol. *ACS Omega* **2022**, *7*, 30908–30919.
- (23) Taufik, A.; Albert, A.; Saleh, R. Sol-gel synthesis of ternary CuO/TiO₂/ZnO nanocomposites for enhanced photocatalytic performance under UV and visible light irradiation. *J. Photochem. Photobiol., A* **2017**, *344*, 149–162.
- (24) Podrojková, N.; Patera, J.; Popescu, R.; Škoviera, J.; Oriňaková, R.; Oriňak, A. Pyrolysis Degradation of Cellulose over Highly Effective ZnO and ZnO-CuO Nanocatalysts. *ChemistrySelect* **2021**, *6*, 4256–4264.
- (25) Shi, S.; Xu, J.; Li, L. Preparation and photocatalytic activity of ZnO nanorods and ZnO/Cu₂O nanocomposites. *Main Group Chem.* **2017**, *16*, 47–55.
- (26) Thambidurai, S.; Gowthaman, P.; Venkatachalam, M.; Suresh, S. Natural sunlight assisted photocatalytic degradation of methylene blue by spherical zinc oxide nanoparticles prepared by facile chemical co-precipitation method. *Optik* **2020**, *207*, 163865.
- (27) Cataño, F. A.; Cáceres, G.; Burgos, A.; Schrebler, R. S. Synthesis and Characterization of a ZnO/CuO/Ag Composite and its Application as a Photocatalyst for Methyl Orange Degradation. *Int. J. Electrochem. Sci.* **2018**, *13*, 9242–9256.
- (28) Nur, A.; Rofi'uddin, J.; Basir, M. A.; Nazriati, N.; Fajaroh, F. Synthesis of ZnO/CuO Composite by The Electrochemical Method in The Acetat Acid Solution. *J. Chem. Eng.* **2018**, *2*, 59–63.
- (29) Pardakhty, A.; Ranjbar, M.; Moshafi, M. H.; Abbasloo, S. A Systematic Study of ZnO/CuO Core/Shell Nanostructures Pegylated by Microwave Assistent Reverse Micelles (RM) Method. *J. Cluster Sci.* **2018**, *29*, 1061–1068.
- (30) Saravanakkumar, D.; Sivaranjani, S.; Kaviyarasu, K.; Ayeshamariam, A.; Ravikumar, B.; Pandiarajan, S.; Veeralakshmi, C.; Jayachandran, M.; Maaza, M. Synthesis and Characterization of ZnOCuO Nanocomposites Powder by Modified Perfume Spray Pyrolysis Method and Its Antimicrobial Investigation. *J. Semicond.* **2018**, *39*, 033001.
- (31) Nithya, K.; Kalyanasundharam, S. Effect of chemically synthesis compared to biosynthesized ZnO nanoparticles using aqueous extract of *C. halicacabum* and their antibacterial activity. *OpenNano* **2019**, *4*, 100024.
- (32) Singh, J.; Dutta, T.; Kim, K.-H.; Rawat, M.; Samddar, P.; Kumar, P. Green synthesis of metals and their oxide nanoparticles: applications for environmental remediation. *J. Nanobiotechnol.* **2018**, *16*, 84.
- (33) Ahmed, S.; Ali, S.; Chaudhry, S. A.; Ikram, S. A review on biogenic synthesis of ZnO nanoparticles using plant extracts and microbes: A prospect towards green chemistry. *J. Photochem. Photobiol., B* **2017**, *166*, 272–284.
- (34) Balraj, B.; Senthilkumar, N.; Siva, C.; Krithikadevi, R.; Julie, A.; Potheher, I. V.; Arulmozhi, M. Synthesis and characterization of zinc oxide nanoparticles using marine *Streptomyces* sp. with its investigations on anticancer and antibacterial activity. *Res. Chem. Intermed.* **2017**, *43*, 2367–2376.
- (35) Demissie, M. G.; Sabir, F. K.; Edossa, G. D.; Gonfa, B. A. Synthesis of zinc oxide nanoparticles using leaf extract of *lippiaadoensis* (koseret) and evaluation of its antibacterial activity. *J. Chem.* **2020**, *2020*, 7459042.
- (36) Raja, A.; Ashokkumar, S.; Pavithra Marthandam, R.; Jayachandiran, J.; Khatiwada, C. P.; Kaviyarasu, K.; Ganapathi Raman, R.; Swaminathan, M. Eco-friendly preparation of zinc oxide nanoparticles using *Tabernaemontana divaricata* and its photocatalytic and antimicrobial activity. *J. Photochem. Photobiol., B* **2018**, *181*, 53–58.
- (37) Hagos, K. M. Synthesis and characterization of ZnO nanoparticles using aqueous extract of *Becium grandiflorum* for antimicrobial activity and adsorption of methylene blue. *Appl. Water Sci.* **2021**, *11*, 45.
- (38) Haque, M. J.; Bellah, M. M.; Hassan, M. R.; Rahman, S.; Zare, M. Synthesis of ZnO nanoparticles by two different methods comparison of their structural, antibacterial, photocatalytic and optical properties. *Nano Express* **2020**, *1*, 010007.
- (39) Hussain, A.; Oves, M.; Alajmi, M. F.; Hussain, I.; Amir, S.; Ahmed, J.; Rehman, T.; El-Seedi, H. R.; Ali, I. Biogenesis of ZnO nanoparticles using *Pandanus odorifer* leaf extract: Anticancer and antimicrobial activities. *RSC Adv.* **2019**, *9*, 15357–15369.
- (40) Sathiyavimal, S.; Vasantharaj, S.; Veeramani, V.; Saravanan, M.; Rajalakshmi, G.; Kaliannan, T.; Al-Misned, F. A.; Pugazhendhi, A. Green chemistry route of biosynthesized copper oxide nanoparticles using *Psidium guajava* leaf extract and their antibacterial activity and effective removal of industrial dyes. *J. Environ. Chem. Eng.* **2021**, *9*, 105033.
- (41) Weldegebrieal, G. K. Photocatalytic and antibacterial activity of CuO nanoparticles biosynthesized using *Verbascum thapsus* leaves extract. *Optik* **2020**, *204*, 164230.
- (42) Mohammadi-Aloucheh, R.; Habibi-Yangjeh, A.; Bayrami, A.; Latifi-Navid, S.; Asadi, A. Green synthesis of ZnO and ZnO/CuO nanocomposites in *Mentha longifolia* leaf extract: Characterization and their application as antibacterial agents. *J. Mater. Sci. Mater. Electron.* **2018**, *29*, 13596–13605.
- (43) Rajith Kumar, C. R.; Betageri, V. S.; Nagaraju, G.; Pujar, G. H.; H S, O.; M S, L. One-pot green synthesis of ZnO-CuO nanocomposite and their enhanced photocatalytic and antibacterial activity. *Adv. Nat. Sci.: Nanosci. Nanotechnol.* **2020**, *11*, 015009.
- (44) Vibitha, B. V.; Anitha, B.; Tharayil, N. J. Green Synthesis of ZnO: CuO Nanocomposites by *Aloe Barbadensis* leaf extract: Structure and Photo Catalytic Properties. *AIP Conf. Proc.* **2020**, *2287*, 020031.
- (45) Elemike, E. E.; Onwudiwe, D. C.; Singh, M. Eco-friendly synthesis of copper oxide, zinc oxide and copper oxide-zinc oxide nanocomposites, and their anticancer applications. *J. Inorg. Organomet. Polym. Mater.* **2020**, *30*, 400–409.
- (46) Wakjira, K.; Negash, L. Germination responses of *Croton macrostachyus* (Euphorbiaceae) to various physico-chemical pretreatment conditions. *South Afr. J. Bot.* **2013**, *87*, 76–83.
- (47) Abraham, F. M.; Ayele, T.; Reta, T.; Wondmagege, T.; Tadesse, E. Experimental evaluation of wound healing activity of *Croton macrostachyus* in rat. *Afr. J. Pharm. Pharmacol.* **2016**, *10*, 832–838.
- (48) Sendeku, W.; Alefew, B.; Mengiste, D.; Seifu, K.; Girma, S.; Wondimu, E.; Bekuma, G.; Verma, D.; Berhane, N. Antibacterial activity of *Croton macrostachyus* against some selected pathogenic bacteria. *Biotechnol. Int.* **2015**, *8*, 11–20.
- (49) Degu, A.; Engidawork, E.; Shibeshi, W. Evaluation of the antidiarrheal activity of the leaf extract of *Croton macrostachyus* Hocsht. ex Del. (Euphorbiaceae) in mice model. *BMC Complementary Altern. Med.* **2016**, *16*, 379.
- (50) Asfaw, M.; Rekik, A.; Worku, G.; Firehiwot, T.; Hirut, B.; Abiy, A.; Eyob, D. Ethno medicinal uses, phytochemistry and antimalarial effect of *Croton macrostachyus* (Bisana): A review. *J. Med. Plants Stud.* **2019**, *7*, 79–88.
- (51) Mohammed, S.; Ahimad, A. Extraction and Phytochemical Determination of Some Selected Traditional Medicinal Plants for Antimicrobial Susceptibility Test, in Adama, Ethiopia. *Int. J. Eng. Sci. Technol.* **2015**, *3*, 1290–1297.

- (52) Salatino, A.; Salatino, M.; Negri, G. Traditional uses, chemistry and pharmacology of Croton species (*Euphorbiaceae*). *J. Braz. Chem. Soc.* **2007**, *18*, 11–33.
- (53) Maroyi, A. Ethnopharmacological uses, phytochemistry, and pharmacological properties of *Croton macrostachyus* Hochst. Ex Delile: A comprehensive review. *Evid. base Compl. Alternative Med.* **2017**, *2017*, 1694671.
- (54) Geyid, A.; Abebe, D.; Debella, A.; Makonnen, Z.; Aberra, F.; Teka, F.; Kebede, T.; Urga, K.; Yersaw, K.; Biza, T.; et al. Screening of some medicinal plants of Ethiopia for their antimicrobial properties and chemical profiles. *J. Ethnopharmacol.* **2005**, *97*, 421–427.
- (55) Bantie, L.; Assefa, S.; Teklehaimanot, T.; Engidawork, E. In vivo antimalarial activity of the crude leaf extract and solvent fractions of *Croton macrostachyus* Hocst. (*Euphorbiaceae*) against *Plasmodium berghei* in mice. *BMC Complementary Altern. Med.* **2014**, *14*, 79.
- (56) Wm, A.; Ya, A.; Ma, M.; et al. In vivo antidiabetic activity of the aqueous leaf extract of *Croton macrostachyus* in alloxan induced diabetic mice. *Pharm. Anal. Acta* **2015**, *6*, 1–5.
- (57) Tala, M. F.; Tan, N. H.; Ndontsa, B. L.; Tane, P. Triterpenoids and phenolic compounds from *Croton macrostachyus*. *Biochem. Syst. Ecol.* **2013**, *51*, 138–141.
- (58) Ababayehu, A.; Mammo, F.; Kibret, B. Isolation and characterization of terpene from leaves of *Croton macrostachyus* (Bissana). *J. Med. Plants Res.* **2016**, *10*, 256–269.
- (59) Liu, F.; Che, Y.; Chai, Q.; Zhao, M.; Lv, Y.; Sun, H.; Wang, Y.; Sun, J.; Zhao, C. Construction of RGO Wrapping Cu₂O/ZnO Heterostructure Photocatalyst for PNP and PAM Degradation. *Environ. Sci. Pollut. Res.* **2019**, *26*, 25286–25300.
- (60) Tantubay, K.; Das, P.; Baskey Sen, M. Ternary reduced graphene oxide-CuO/ZnO nanocomposite as a recyclable catalyst with enhanced reducing capability. *J. Environ. Chem. Eng.* **2020**, *8*, 103818.
- (61) Gawade, V. V.; Gavade, N. L.; Shinde, H. M.; Babar, S. B.; Kadam, A. N.; Garadkar, K. M. Green synthesis of ZnO nanoparticles by using *Calotropis procera* leaves for the photodegradation of methyl orange. *J. Mater. Sci.* **2017**, *28*, 14033–14039.
- (62) Naseri, A.; Samadi, M.; Mahmoodi, N. M.; Pourjavadi, A.; Mehdipour, H.; Moshfegh, A. Z. Tuning composition of electrospun ZnO/CuO nanofibers: toward controllable and efficient solar photocatalytic degradation of organic pollutants. *J. Phys. Chem. C* **2017**, *121*, 3327–3338.
- (63) Subramaniyan, A.; Thirupathi, S.; Sathath, M. I.; Kannan, M. Investigation on band gap of CuO-ZnO nanocomposite thin films and stability of CuO-ZnO nanofluids. *J. Nanoelectron. Optoelectron.* **2018**, *13*, 1366–1373.
- (64) Tsege, E. L.; Cho, S. K.; Tufa, L. T.; Tran, V. T.; Lee, J.; Kim, H.; Hwang, Y. Scalable and inexpensive strategy to fabricate CuO/ZnO nanowire heterojunction for efficient photoinduced water splitting. *J. Mater. Sci.* **2018**, *53*, 2725–2734.
- (65) Guo, F.; Huang, X.; Chen, Z.; Cao, L.; Cheng, X.; Chen, L.; Shi, W. Construction of Cu₃P-ZnSnO₃-g-C₃N₄ p-n-n heterojunction with multiple built-in electric fields for effectively boosting visible-light photocatalytic degradation of broad-spectrum antibiotics. *Sep. Purif. Technol.* **2021**, *265*, 118477.
- (66) Ullah, H.; Mushtaq, L.; Ullah, Z.; Fazal, A.; Khan, A. M. Effect of vegetable waste extract on microstructure, morphology, and photocatalytic efficiency of ZnO-CuO nanocomposites. *Inorg. Nano-Met. Chem.* **2021**, *51*, 963–975.
- (67) Renuka, L.; Anantharaju, K. S.; Vidya, Y. S.; Nagaswarupa, H. P.; Prashantha, S. C.; Nagabhushana, H. Synthesis of Sunlight Driven ZnO/CuO Nanocomposite: Characterization, Optical, Electrochemical and Photocatalytic Studies. *Mater. Today Proc.* **2017**, *4*, 11782–11790.
- (68) Ben Salem, B.; Essalah, G.; Ben Ameer, S.; Duponchel, B.; Guermazi, H.; Guermazi, S.; Leroy, G. Synthesis and comparative study of the structural and optical properties of binary ZnO-based composites for environmental applications. *RSC Adv.* **2023**, *13*, 6287–6303.
- (69) Mageshwari, K.; Nataraj, D.; Pal, T.; Sathyamoorthy, R.; Park, J. Improved photocatalytic activity of ZnO coupled CuO nanocomposites synthesized by reflux condensation method. *J. Alloys Compd.* **2015**, *625*, 362–370.
- (70) Zelekew, O. A.; Fufa, P. A.; Sabir, F. K.; Duma, A. D. Water hyacinth plant extract mediated green synthesis of Cr₂O₃/ZnO composite photocatalyst for the degradation of organic dye. *Heliyon* **2021**, *7*, No. e07652.
- (71) Rini, N. P.; Istiqomah, N. I.; Sunarta; Suharyadi, E. Enhancing photodegradation of methylene blue and reusability using CoO/ZnO composite nanoparticles. *Case Stud. Chem. Environ. Eng.* **2023**, *7*, 100301.